



Numerical Solution of the Radiation Transport Equation at an Air-Water Interface for a Stratified Medium

K. Peter Judd^{1*} and Robert A. Handler²

¹ Naval Research Laboratory, Optical Sciences Division, Washington, DC, United States, ² Department of Mechanical Engineering, George Mason University, Fairfax, VA, United States

OPEN ACCESS

Edited by:

David B. Go,
University of Notre Dame,
United States

Reviewed by:

Tengfei Luo,
University of Notre Dame,
United States
Tanvir I. Farouk,
University of South Carolina,
United States

*Correspondence:

K. Peter Judd
kyle.judd@nrl.navy.mil

Specialty section:

This article was submitted to
Thermal and Mass Transport,
a section of the journal
Frontiers in Mechanical Engineering

Received: 27 October 2018

Accepted: 11 January 2019

Published: 18 February 2019

Citation:

Judd KP and Handler RA (2019)
Numerical Solution of the Radiation
Transport Equation at an Air-Water
Interface for a Stratified Medium.
Front. Mech. Eng. 5:1.
doi: 10.3389/fmech.2019.00001

This paper is a continuation of previous work that analytically examined the strength of radiation leaving an air-water interface. The approach here is to numerically integrate the radiation transport equation in order to capture the non-linear features of the problem, and also to include more realistic models for the thermal boundary layer. The radiation intensity of the photons emitted from the interface, relative to that of thermal radiation at the temperature of the interface, is defined here as the *signal*. This signal was computed for constant surface temperature and constant heat flux boundary conditions. As expected, the numerical computations show that the signal increased as the air-water temperature difference increased. The results are shown to form a hierarchy of signal strengths based on the chosen thermal stratification model. However, for both boundary conditions, the numerical results for a linear temperature profile compared very favorably with the simplified analytical linearized model over the thermal wavebands of 3–5 and 8–14 microns. In addition, the linearized model compared favorably with the most realistic models of thermal stratification.

Keywords: infrared radiation, air-water interface, radiation transport equation, thermal layer, stratified medium

INTRODUCTION

The goal of determining the physical mechanisms responsible for the transport of mass, momentum and energy across the air-sea interface has driven research in recent years since such knowledge may, among other things, contribute to more accurate estimates for the evolution of the climate of the earth. Although bulk parameterization provides estimates of the net transport of heat and gases, their transport is ultimately controlled by thin temperature and concentration boundary layers that form at the air-sea boundary (Fairall et al., 1996). In recent years, however, significant efforts have succeeded in uncovering the microphysics controlling thermal and gas fluxes by employing controlled laboratory experiments (Katsaros et al., 1977; Jahne et al., 1987; Handler et al., 2001; Handler and Smith, 2011).

More specifically, atmospheric accumulation of greenhouse gases such as CO₂, has attracted great attention in recent decades. The rate at which such gases are taken up by the oceans continue to remain somewhat uncertain despite significant recent research (Wanninkhof, 1992, 2014). The determination of these gas fluxes is a difficult task, but in recent decades, it was pointed out that gas flux could be estimated from heat flux measurements (Atmane et al., 2004). This can be achieved by measuring the heat flux, and using the ratio of gas Schmidt number to the Prandtl number to estimate gas flux. If such an analogy between heat and gas flux is valid, then remote infrared (IR)

measurements of the ocean surface could be used to extract heat flux and then converted to gas flux. In addition, such a method would allow large regions of the ocean to be mapped by aircraft or satellite, giving unprecedented maps of oceanic gas flux. In addition, heat flux is obviously an important quantity, in and of itself.

Direct measurement of the temperature profile at an air-water interface using probes such as thermocouples and fast response thermistors is difficult owing to the extremely small thickness of these thermal layers, typically from 0.1 to 1 mm. The temperature difference across these layers, often referred to as the *cool-skin*, can be as large as $T = 1.0 \text{ K}$ (Katsaros et al., 1977). However, recent advances in remote sensing hardware, in particular infrared (IR) imagers, have stimulated the development of unique approaches to extracting heat fluxes from image based techniques (Garbe et al., 2004). Numerical simulations have also provided insight into the small-scale turbulent dynamics that determine these fluxes (Handler et al., 1999; Leighton et al., 2003; Nagaosa and Handler, 2003, 2012; Handler and Zhang, 2013; Herlina and Wissink, 2014; Fredriksson et al., 2016a,b). We point out here that the very thin thermal boundary layer at the air-sea interface is formed as a result of a competition between upward heat flux out of the interface, which tends to increase the thermal layer thickness, and subsurface turbulence, which tends to decrease it as a result of the surface renewal of bulk fluid. The detailed physics of this is well-known, and is well-described elsewhere (Jahne et al., 1989; Handler et al., 1999, 2001; Atmane et al., 2004; Handler and Zhang, 2013).

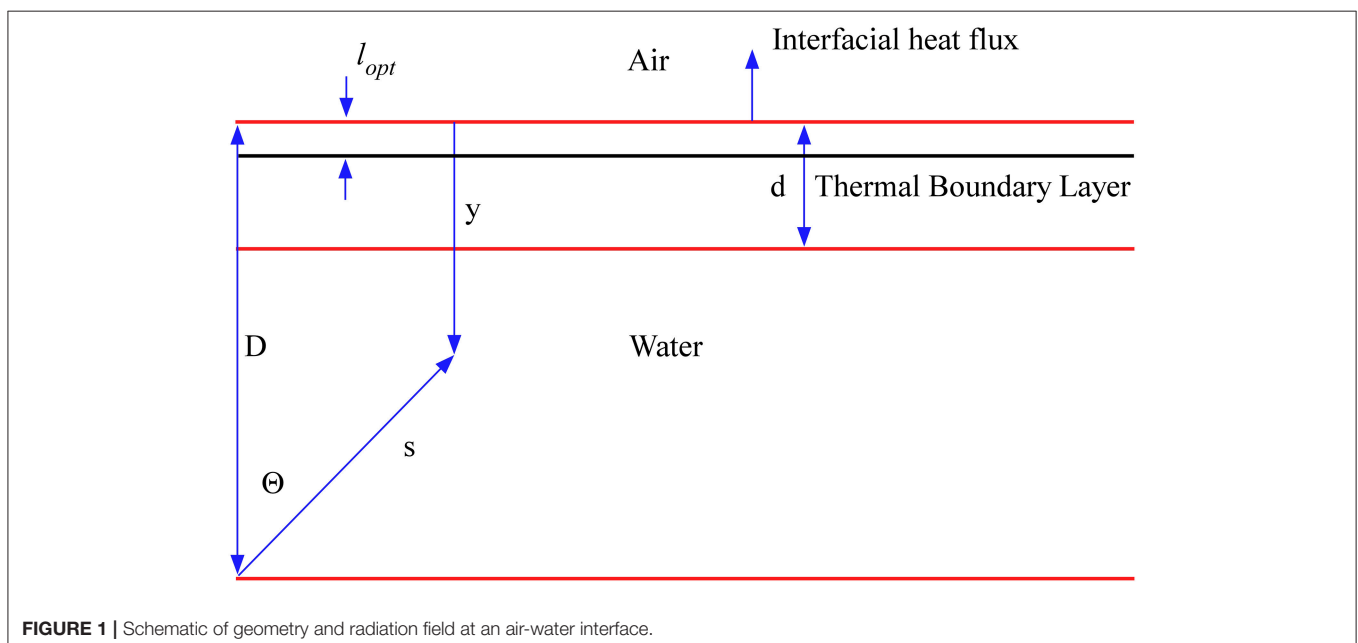
Past and recent efforts have used both aircraft and satellite platforms equipped with radiometers and/or thermal imagers to produce sea-surface temperature products in addition to attempts to determine oceanic heat flux. As heat flux may serve as a proxy for gas flux (Jahne et al., 1987), having a robust instrument and atmospheric sounding retrieval technique could provide wide area maps of simultaneously acquired heat and

gas transport. Early efforts for remotely extracting heat flux by McAlister and McLeish (1970) and McAlister et al. (1971) exploit the varying optical depth of thermal radiation within the aqueous layer in wavelength bands that are transparent to the atmosphere (Downing and Williams, 1975). This approach was revisited some 30 years later by McKeown et al. (1995) and McKeown and Leighton (1999), who performed laboratory experiments using band-pass filters and an imaging array.

Consistent with the goals stated above, and as discussed in Handler and Judd (2018), our motivation is to accurately estimate the magnitude and direction of the radiation emerging from a thermally stratified medium. In that work, the problem was made tractable by employing simplifying assumptions (e.g., ignoring surface waves, scattering, assuming a linear temperature profile, and taking only the first term in a series expansion of the Planck spectrum). This allowed the governing radiation transport equation to be solved exactly. The result provides the deviation of the surface radiation intensity from the Planck spectrum in terms of three non-dimensional numbers. However, thermal profiles are found to have a non-linear character, typically varying as a decaying exponential over the boundary layer thickness. To elucidate the nature of this non-linear stratification, in the present work we remove the previously employed linearity assumptions, and estimate the surface radiation for several more *realistic* thermal profiles (Smith et al., 2001). This requires the numerical integration of the transport equation. Results are obtained for both a constant temperature surface boundary condition, and the more frequently encountered constant heat flux condition.

RADIATION TRANSPORT EQUATION IN A STRATIFIED MEDIUM

The details of the development of the governing equation and its solution can be found in Handler and Judd (2018); however,



for completeness we briefly define the problem. The radiation transport equation (RTE) for an emitting and absorbing medium takes the form (Chandrasekhar, 1960):

$$\frac{dI}{ds} = -k\rho I + \rho j \tag{1}$$

where I is the radiation intensity, s is the coordinate associated with a spatial direction, k is the opacity, ρ is the density of the medium, and j is the emission coefficient. From local thermodynamic equilibrium j takes the form:

$$j = kB(T, \lambda) \tag{2}$$

where $B(T, \lambda)$ is the Planck spectrum and is given by:

$$B(T, \lambda) = \frac{C_1}{\lambda^5} \left[\frac{1}{e^{(C_2(\lambda)/T)} - 1} \right] \tag{3}$$

The radiation constants take the form, $C_1 = 2hc^2$, $C_2(\lambda) = hc/\lambda k_b$, h is Planck's constant, c is the speed of light, λ is the wavelength of radiation, k_b is the Boltzmann's constant, and T is the absolute temperature. **Figure 1** shows the geometry considered for the radiation field in a stratified medium, which represents an aqueous layer bounded above by an air mass. The temperature in the aqueous layer is assumed to be stratified in planes parallel to the air-water interface defined at $y = 0$.

As shown in **Figure 1**, three length scales are of importance: (1) The thermal layer thickness d , (2) An outer scale D , and (3) the optical depth, l_{opt} , of the medium. For future reference, we define a linearly varying temperature field (Handler and Judd, 2018) given by:

$$T(y) = \begin{cases} \frac{\Delta T}{d}y + T_0, & 0 \leq y < d \\ T_d, & d \leq y < D \end{cases} \tag{4}$$

where $\Delta T = T_d - T_0$, $T_0 = T(0)$ is the temperature at the air-water interface, and $T_d = T(d)$. The coordinate y can be related to s giving $y = D - s \cos(\theta)$. Inserting this into Equation (1), and integrating yields:

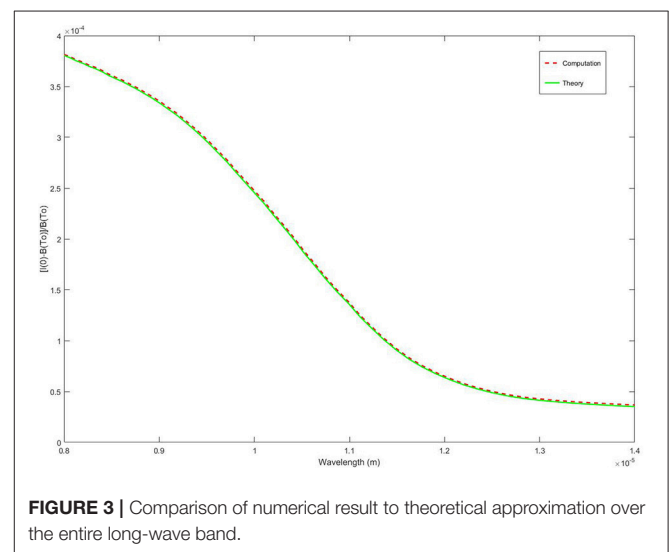
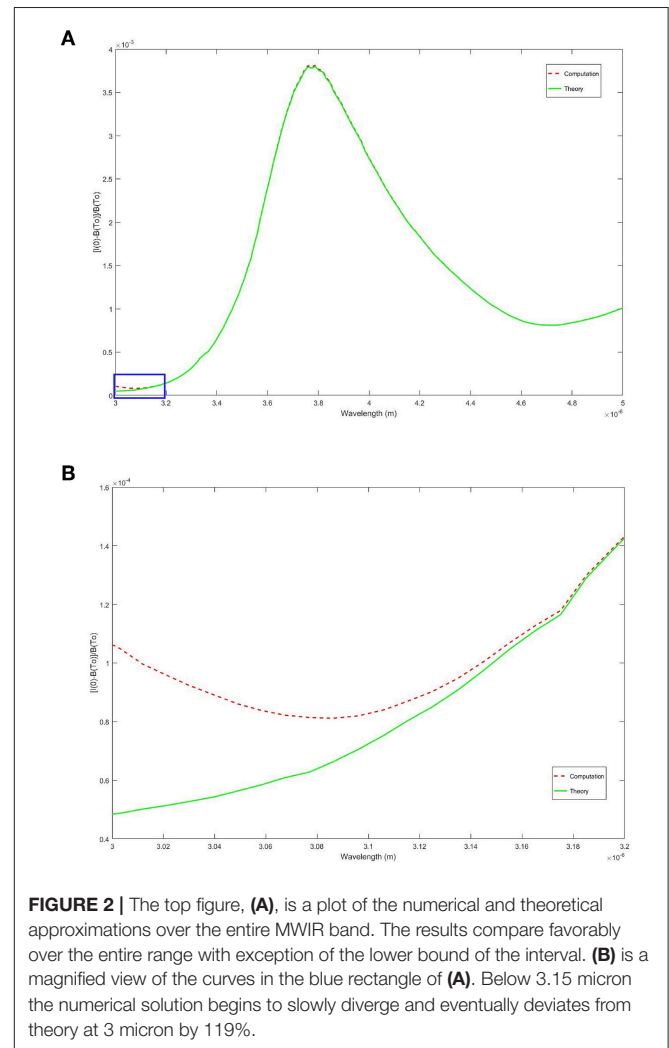
$$I(y) = I_D e^{\frac{\beta(\lambda)}{\cos\theta}(y-D)} + \frac{\beta(\lambda)}{\cos\theta} \int_y^D B(T, \lambda) e^{\frac{\beta(\lambda)}{\cos\theta}(y-\bar{y})} d\bar{y}, \tag{5}$$

where I_D and is the radiation intensity at $y = D$.

NUMERICAL SOLUTION OF THE RTE IN A STRATIFIED MEDIUM WITH A LINEAR TEMPERATURE PROFILE

As previously noted, no known closed form solution exists for the general integral equation, Equation (5), for the given temperature profile, Equation (4). Here solutions to this expression will be obtained using a numerical approach. These will then be compared to the approximate solution developed for small temperature perturbations. In Equation (5) the term $\beta(\lambda) = \frac{1}{l_{opt}(\lambda)}$ is the reciprocal of the wavelength dependent optical depth. In this work, we examine radiation in two commonly defined

thermal wavelength bands: the 3–5 μm (mid-wave or MWIR) and the 8–14 μm (long-wave or LWIR) bands. The optical depth is rather shallow for both bands, varying from 1 to 90 microns in



the MWIR band and 3–19 microns in the LWIR band (Downing and Williams, 1975). In these calculations, we will use an aqueous thermal boundary layer thickness of $d = 1$ mm, and outer layer of $D = 0.5$ m, and a surface temperature $T(y = 0) = T_0 = 300$ K.

The radiation intensity at the interface, $y = 0$, is as follows:

$$I(0) = I_D e^{\frac{\beta(\lambda)}{\cos\theta}(-D)} + \frac{\beta(\lambda)}{\cos\theta} \int_0^D B(T, \lambda) e^{\frac{\beta(\lambda)}{\cos\theta}(-y)} dy. \quad (6)$$

For our purposes, we consider radiation in a direction perpendicular to the interface ($\theta = 0$) such that the signal is maximal (Zel'dovich and Raizer, 1966). With the assumption that the water depth is effectively infinite ($\frac{D}{d} \gg 1$), and that $\frac{D}{l_{opt}} \gg 1$, we obtain:

$$I(0; \lambda) = \beta(\lambda) \int_0^D B(T(\bar{y}), \lambda) e^{\beta(\lambda)(-y)} d\bar{y}. \quad (7)$$

For clarity, the dependence of the radiation intensity on wavelength, and the Planck spectrum on temperature has been indicated. We initially addressed Equation (7) numerically using an in-house written composite Simpson's 3/8 rule integration scheme thus permitting greater flexibility in controlling the governing input parameters compared to a commercial computational package. The thermal stratification in these computations is linear as defined in Equation (4), so as to compare with theory (Handler and Judd, 2018):

$$\frac{I(0) - B(T_0)}{B(T_0)} = K_1 K_2 K_3 \cos\theta \quad (8)$$

$$\text{where } K_1 = \frac{C_2}{T_0}, K_2 = \frac{\Delta T}{T_0}, \text{ and } K_3 = \frac{l_{opt}}{d}.$$

We define the relative signal strength as \bar{I} where $\bar{I} = [I(0) - B(T_0)]/B(T_0)$. **Figure 2A** shows the comparison of theory and computation for the excess of surface radiation intensity with respect to the Planck spectrum in the 3–5 micron waveband. As in Handler and Judd (2018) we will refer to this

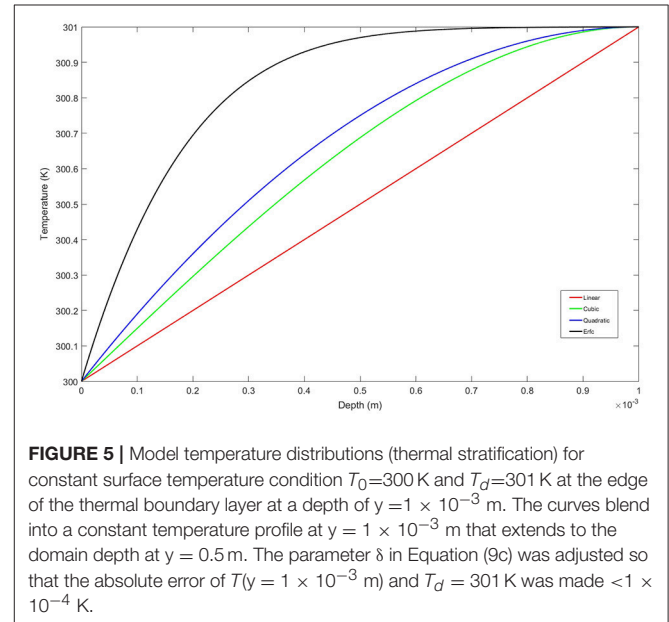


FIGURE 5 | Model temperature distributions (thermal stratification) for constant surface temperature condition $T_0=300$ K and $T_d=301$ K at the edge of the thermal boundary layer at a depth of $y = 1 \times 10^{-3}$ m. The curves blend into a constant temperature profile at $y = 1 \times 10^{-3}$ m that extends to the domain depth at $y = 0.5$ m. The parameter δ in Equation (9c) was adjusted so that the absolute error of $T(y = 1 \times 10^{-3}$ m) and $T_d = 301$ K was made $< 1 \times 10^{-4}$ K.

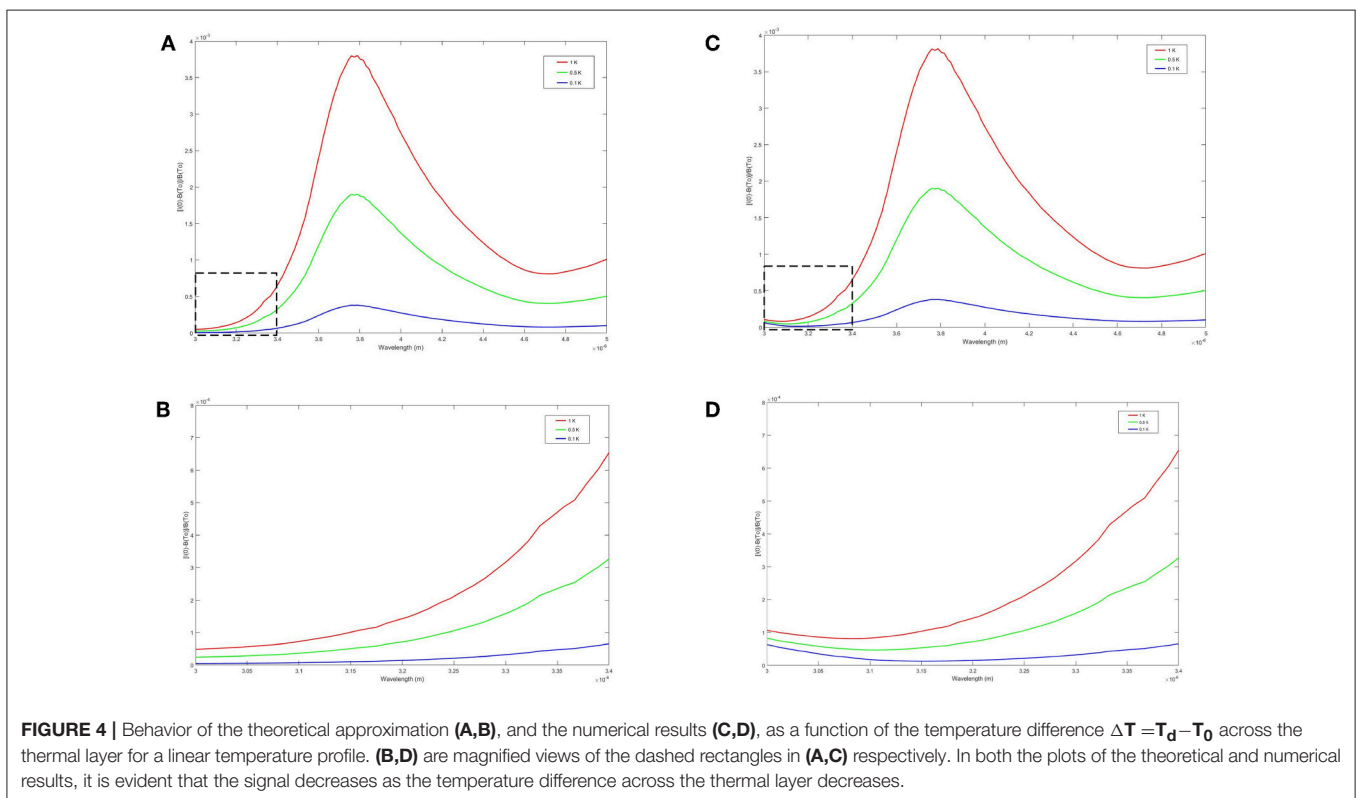


FIGURE 4 | Behavior of the theoretical approximation (A,B), and the numerical results (C,D), as a function of the temperature difference $\Delta T = T_d - T_0$ across the thermal layer for a linear temperature profile. (B,D) are magnified views of the dashed rectangles in (A,C) respectively. In both the plots of the theoretical and numerical results, it is evident that the signal decreases as the temperature difference across the thermal layer decreases.

quantity as the *signal*. The numerical results agree well over the band with exception of the range $\lambda \lesssim 3.15 \mu\text{m}$, the blue rectangle in the figure. **Figure 2B** is an exploded view of this region where the numerical result deviates as it approaches the lower bound of the mid-wave band. We speculate that this behavior is related to the very small optical depth ($l_{opt}(\lambda) < 3\mu\text{m}$) over this wavelength range, resulting in difficulty in resolving the region with uniform grid spacing. An increase in the number of node points in the computational scheme lessened the deviation from the theory, but did not completely remove the effect. To fully resolve this region we employed an adaptive scheme (Gauss-Kronrod quadrature) from MATLAB R2016a (MathWorks Inc., Natick, MA, USA). Application of the adaptive scheme and results are discussed in the next section where more realistic thermal boundary layer profiles are considered. The same composite Simpson's rule was applied to the long-wave range in **Figure 3**. The resulting theoretical and numerical curves compare favorably over the entire waveband. This is likely in part due to the fact that unlike the optical depths for mid-wave radiation which decrease below $3 \mu\text{m}$, long-wave optical depths are $l_{opt}(\lambda) \geq 3\mu\text{m}$ over the entire waveband.

Finally, we address the behavior of the theoretical and numerical results as a function of the temperature difference, $\Delta T = T_d - T_0$, across the thermal layer. The temperature was varied over the range of values given by $\Delta T = 0.1 \text{ K}, 0.5 \text{ K}, 1.0 \text{ K}$, with all other variables fixed as previously stated. It is evident from **Figure 4** (and Equation 8) that the theoretical *signal* decreases with decreasing temperature difference.

Although we have not presented the results for the long-wave band, a similar decrease in signal strength was observed for both the theoretical and computational results as the temperature difference was decreased.

NON-LINEAR STRATIFICATION

The theoretical and computational results for the linear profile validates the approach used here, so that it can now be employed to determine the surface radiation resulting from more realistic thermally stratified layers. Here we consider two surface conditions; a constant surface temperature and the more

frequently encountered constant surface heat flux condition (Csanady, 2001). Several temperature distributions, including the linear profile in Equation (4) are examined.

The thermal boundary layers for the constant temperature surface condition are listed in Equations (9a-d). The definition of the symbol i used in 9c and 10d is provided in **Appendix**, additional details can be found in Gautschi (1961).

$$T(y) = \begin{cases} \left(\frac{\Delta T}{d}\right)\left[2y - \frac{y^2}{d}\right] + T_0, & 0 \leq y \leq d & (a) \\ \left(\frac{\Delta T}{2d}\right)\left[3y - \frac{y^3}{d^2}\right] + T_0, & 0 \leq y \leq d & (b) \\ -\Delta T 4i^2 \operatorname{erfc}\left(\frac{\sqrt{\pi}}{4i}y\right) + T_d, & 0 \leq y \leq d & (c) \\ T_d, & d \leq y \leq D & (d) \end{cases} \quad (9)$$

In **Figure 5** each of these thermal profiles [Equations (4, 9a-c)] are determined with $T(y=0) = T_0 = 300 \text{ K}$ and $T(y=d) = T_d = 301 \text{ K}$ where $d=1 \times 10^{-3} \text{ m}$ is the edge of the thermal layer. Equations (9a,b) are standard polynomial approximations (Kays and Crawford, 1993). The temperature distribution in equation (9c) incorporates a surface renewal model (Liu and

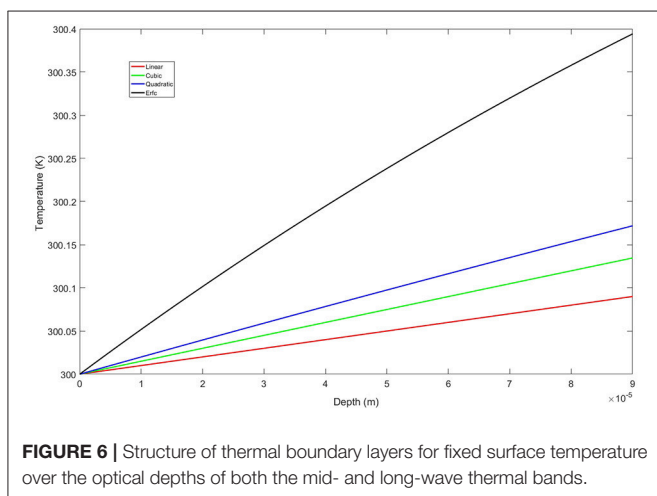


FIGURE 6 | Structure of thermal boundary layers for fixed surface temperature over the optical depths of both the mid- and long-wave thermal bands.

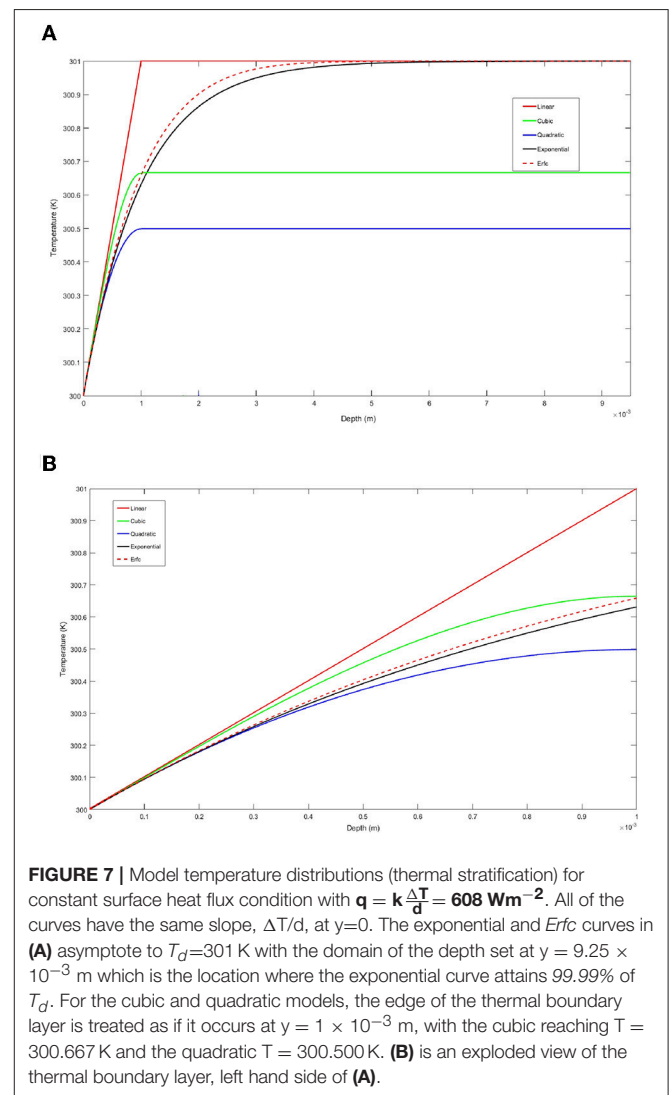


FIGURE 7 | Model temperature distributions (thermal stratification) for constant surface heat flux condition with $q = k \frac{\Delta T}{d} = 608 \text{ Wm}^{-2}$. All of the curves have the same slope, $\Delta T/d$, at $y=0$. The exponential and *Erfc* curves in **(A)** asymptote to $T_d=301 \text{ K}$ with the domain of the depth set at $y = 9.25 \times 10^{-3} \text{ m}$ which is the location where the exponential curve attains 99.99% of T_d . For the cubic and quadratic models, the edge of the thermal boundary layer is treated as if it occurs at $y = 1 \times 10^{-3} \text{ m}$, with the cubic reaching $T = 300.667 \text{ K}$ and the quadratic $T = 300.500 \text{ K}$. **(B)** is an exploded view of the thermal boundary layer, left hand side of **(A)**.

Businger, 1975; Katsaros et al., 1977), adapted for a constant surface temperature boundary condition. We note that for fixed temperature boundary conditions, the slope for each of the profiles at and near the surface ($y = 0$) varies from curve-to-curve as shown in **Figures 5, 6**. This hierarchy of thermal stratification becomes important when comparing the results of the signal strength and will be discussed in the next section.

We also consider thermal profiles corresponding to a constant surface flux, $\frac{dT(y=0)}{dy} = \text{constant}$, with $q = k \frac{\Delta T}{d} = 608 \text{ Wm}^{-2}$ which is approximately the heat flux obtain in the experiments by Handler and Smith (2011) for a wind speed of 3 ms^{-1} . These temperature profiles are given by:

$$T(y) = \begin{cases} \left(\frac{\Delta T}{d}\right) \left[y - \frac{y^2}{2d}\right] + T_0 & , 0 \leq y \leq d \quad (a) \\ \left(\frac{\Delta T}{d}\right) \left[y - \frac{y^3}{3d^2}\right] + T_0 & , 0 \leq y \leq d \quad (b) \\ -\Delta T \exp\left(\frac{-y}{\delta}\right) + T_d & , 0 \leq y \leq d \quad (c) \\ -\Delta T 6i^3 \operatorname{erfc}\left(\frac{2}{3\sqrt{\pi}\delta}y\right) + T_d & , 0 \leq y \leq d \quad (d) \\ T_d & , d \leq y \leq D \quad (e) \end{cases} \quad (10)$$

The exponential and *Erfc* curves in **Figure 7A** asymptote to $T_d = 301 \text{ K}$ with the domain depth set at $y = 9.25 \times 10^{-3} \text{ m}$, which is the location where the exponential curve attains 99.99% of T_d . For the cubic and quadratic models, the edge of the thermal boundary layer is treated as if it occurs at $y = 1 \times 10^{-3} \text{ m}$, with the cubic reaching $T = 300.667 \text{ K}$ and the quadratic $T = 300.500 \text{ K}$. **Figure 7B** shows that the linear temperature distribution has the largest net change in temperature over the thermal boundary layer and bounds the

profiles. Upon closer examination of the very near-surface region shown in **Figure 8**, we see that all the profiles are nearly linear, with the linear profile slightly higher than all the others.

RESULTS FOR NON-LINEAR STRATIFICATION

To determine the surface radiation intensity, the above temperature profiles were substituted into Equation (7), and the MATLAB *Integral* function was used to perform the integration. This is a global adaptive quadrature routine with the relative and absolute tolerances set to 10^{-8} and 10^{-12} , respectively. **Figure 9A** shows the *signal* for the constant temperature boundary condition with a fixed temperature change of $\Delta T = 1.0 \text{ K}$ across the surface layer over the mid-wave band for the various profiles. Here we repeat the computation for the linear profile and compare it with the theoretical result (**Figure 9B**). It is evident that the curves match well over the entire range of wavelengths, even below $\lambda \approx 3.15 \mu\text{m}$ where large deviations from the theoretical values were previously observed (see **Figure 2B**). Most notably in **Figure 9A**, as the temperature profile becomes fuller, the resulting gradient is steeper and the *signal* tends to increase in magnitude. The hierarchy from smallest to largest overall *signal* as a function of temperature distribution is as follows; linear, cubic, quadratic, and *Erfc* with the peak of all the curves occurring at $\lambda \approx 3.8 \mu\text{m}$. This is not unexpected as the optical depth is largest, $\sim 90 \times 10^{-6} \text{ m}$, at this location and drops off on either side of the peak. A similar behavior was observed in the *signal* curve for the long-wave band, **Figure 10**, with the peak occurring at the lower bound of the waveband at $\lambda \approx 8 \mu\text{m}$,

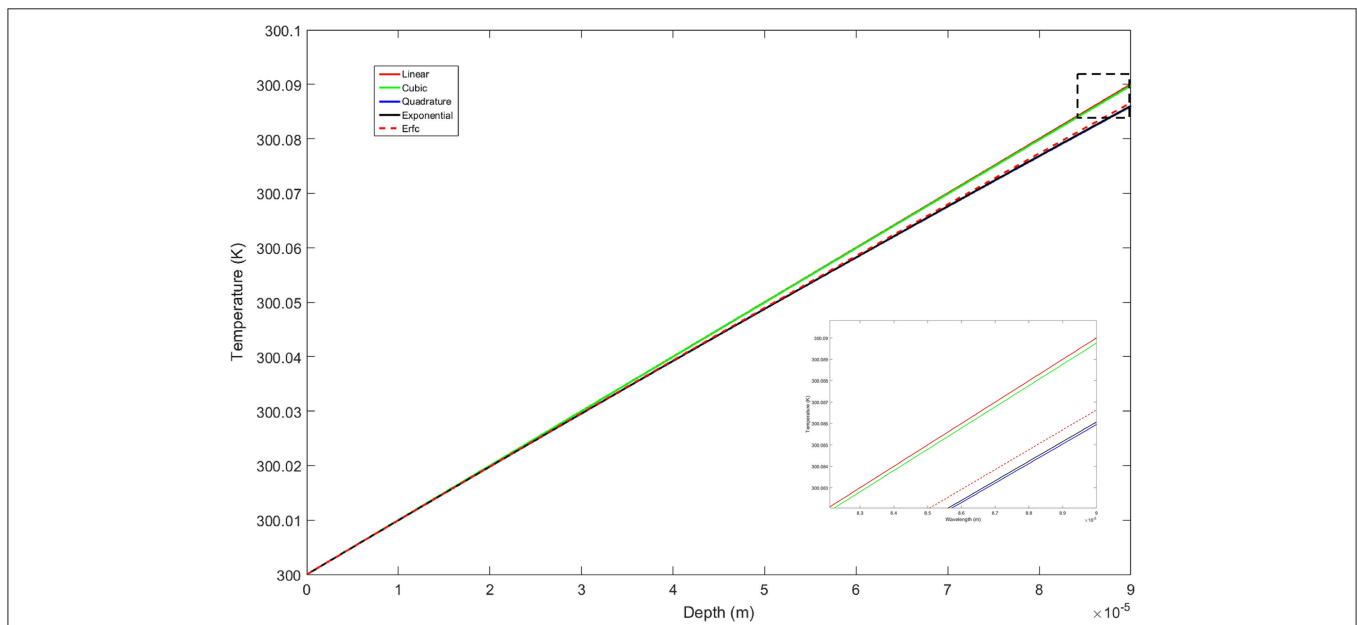
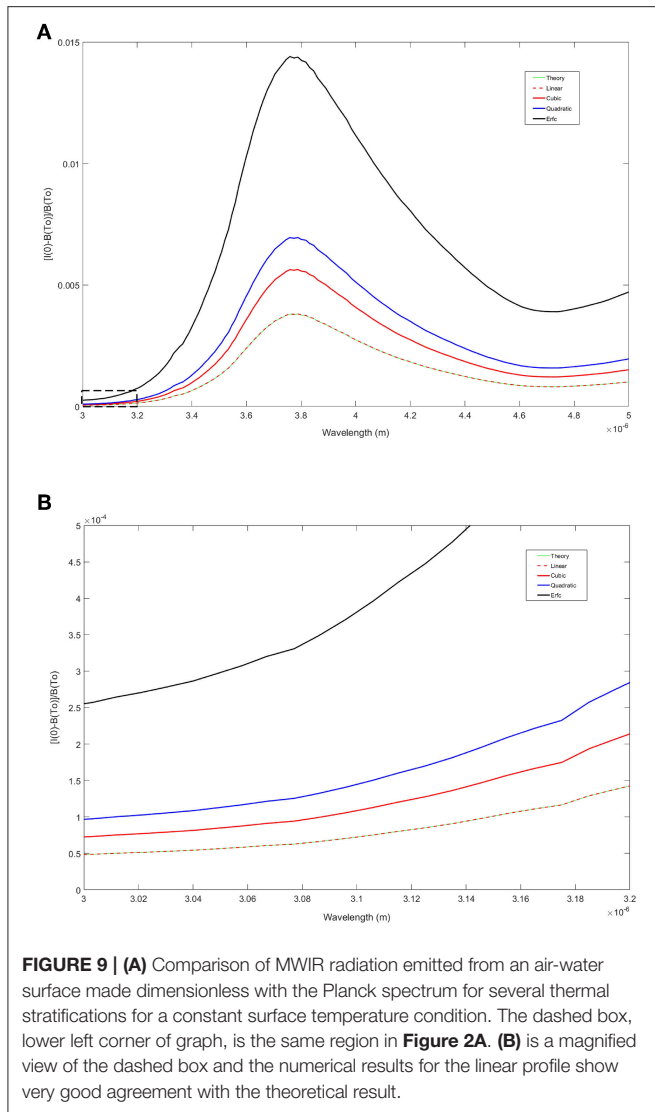
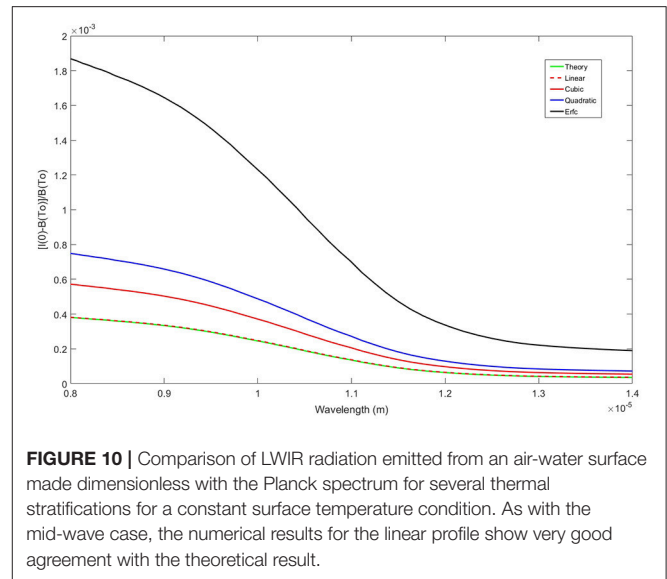


FIGURE 8 | Structure of the thermal boundary layers for fixed heat flux extending over the optical depths for both the mid- and long-wave thermal bands. The inset is of the dashed rectangle in the upper right of the curve and shows the hierarchy of the temperature profiles.



which is again where the optical depth attains its largest value $\sim 19 \times 10^{-6}$ m.

In general, an increase in the *signal* of the emitted surface radiation for both the mid-wave and long-wave bands is associated with the temperature profile that increases in magnitude the most over their respective optical depths. In the case of the constant surface temperature, **Figure 5**, the *Erfc* distribution dominates all other profiles with representative increases in temperature of $\Delta T = 0.4$ K at a depth of 90×10^{-6} m and $\Delta T = 0.1$ K at 19×10^{-6} m. For comparison the next largest profile is the quadratic with increases in temperature of $\Delta T = 0.17$ K at a depth of 90×10^{-6} m and $\Delta T = 0.04$ K at 19×10^{-6} m. The change in relative signal strength \bar{I} at $\lambda \approx 3.8 \mu\text{m}$, the wavelength with the largest optical depth in the mid-wave band, between the *Erfc* and quadratic profile is $\Delta \bar{I} = \bar{I}_{Erfc} - \bar{I}_{Quad} = 0.00745$, implying that the *Erfc* signal is almost double that of the quadratic. Likewise for the long-wave band at its maximum optical depth ($\lambda \approx 8 \mu\text{m}$), $\Delta \bar{I} = 0.001120$, implying that the *Erfc* signal is 2.5x that of the quadratic.



For the constant heat flux boundary condition, the relative changes in signal strength are less significant, and in fact the linear profile which resulted in the weakest signal for the constant temperature case now produces the strongest, **Figures 11, 12**. Upon closer examination of the temperature profiles, all of them are nearly linear over the optical depth layer for the mid- and long-wave bands (**Figure 8**). Representative changes in temperature of the linear profile, which provides an upper bound for the family of temperature distributions, are $\Delta T = 0.0899$ K at a depth of 90×10^{-6} m and $\Delta T = 0.0189$ K at 19×10^{-6} m. For purposes of comparison, we take a closer look at the temperature and signal variations between the linear profile and the quadratic model which provides a lower bound for the family of temperature distributions. The increase in temperature of the quadratic profile at 90×10^{-6} m is $\Delta T = 0.0859$ K and $\Delta T = 0.0187$ K at 19×10^{-6} m. The resulting change in relative signal strength at $\lambda \approx 3.8 \mu\text{m}$ is $\Delta \bar{I} = \bar{I}_{Lin} - \bar{I}_{Quad} = 3.460 \times 10^{-4}$, implying that the linear signal is $\sim 10\%$ larger than the quadratic. For the long-wave band at $\lambda \approx 8 \mu\text{m}$ the change in signal is $\Delta \bar{I} = 7.30 \times 10^{-6}$ implying the linear signal is $\sim 2\%$ larger than the quadratic.

SUMMARY AND CONCLUSIONS

We have numerically addressed the problem of determining the radiation intensity or *signal* of thermal infrared radiation emitted from an air-water interface for a thermally stratified aqueous layer. Our effort is motivated by the possibility of determining, by solely passive means, the transport of heat and gas from the air-sea interface, a problem of importance in determining global climate evolution (Wanninkhof, 1992, 2014).

The approach taken was to numerically integrate the radiation transport equation with a linearly varying temperature field, validate the results with a previously derived analytical

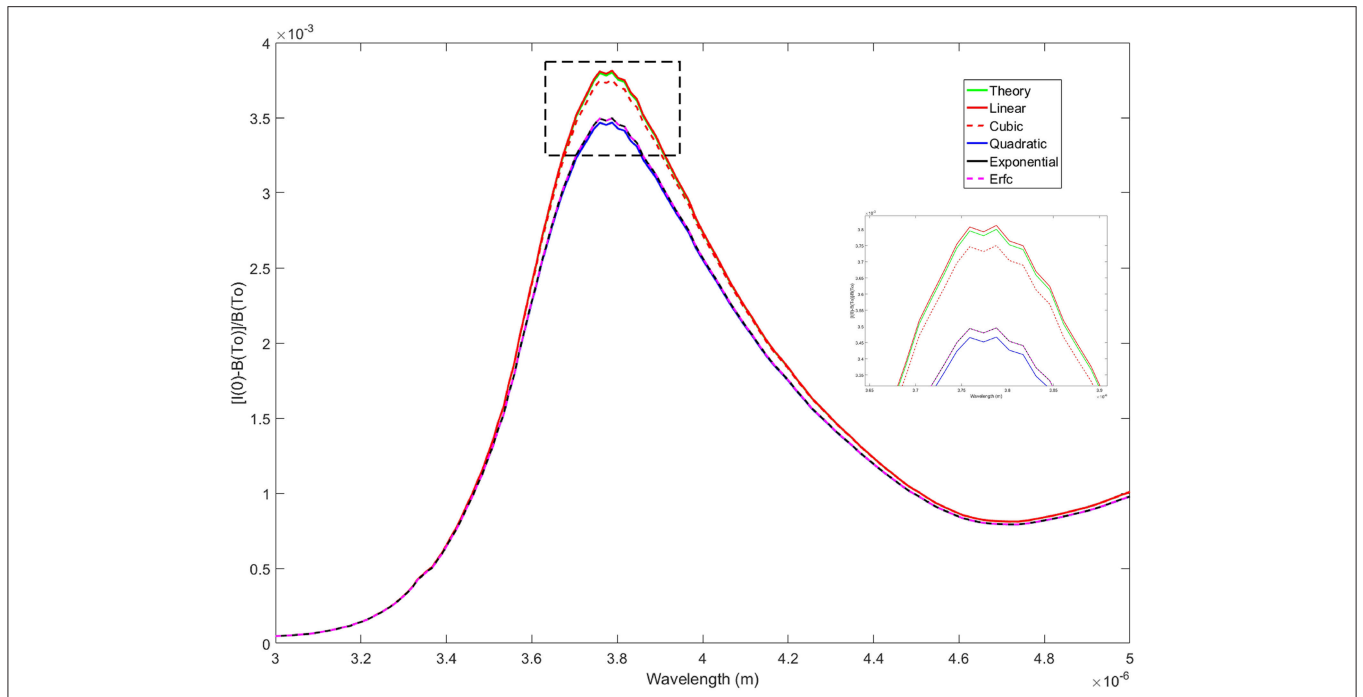


FIGURE 11 | Comparison of MWIR radiation emitted from an air-water surface made dimensionless with the Planck spectrum for several thermal stratifications for a constant surface heat flux condition. The inset is a magnified view of the dashed rectangle surrounding the peak of the curves at $\lambda \approx 3.8 \times 10^{-6}$ m.

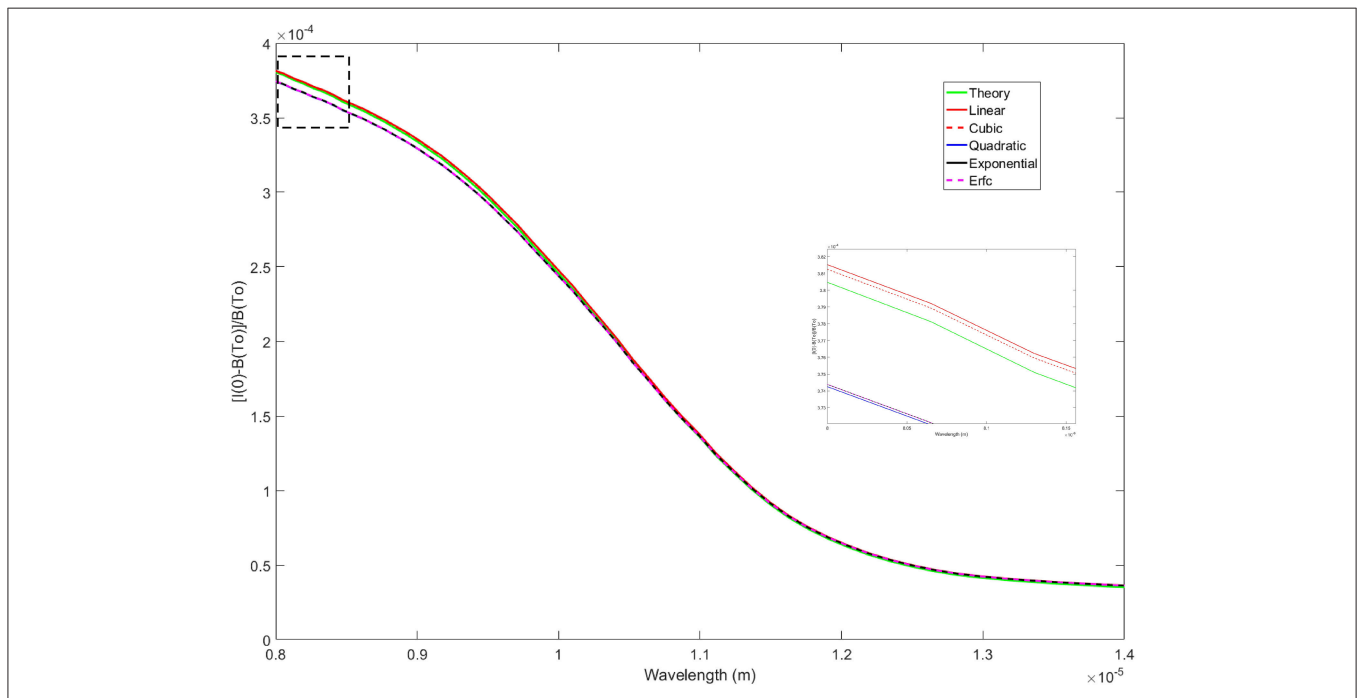


FIGURE 12 | Comparison of LWIR radiation emitted from an air-water surface made dimensionless with the Planck spectrum for several thermal stratifications for a constant surface temperature condition. The inset is a magnified view of the dashed rectangle surrounding the curves at $\lambda \approx 8 \times 10^{-6}$ m.

expression, and to go further by using a family of more realistic thermal boundary layer profiles. Results for both constant temperature and constant heat flux boundary conditions were

obtained. In order to retain the non-linear features of the problem, few simplifications were imposed beyond making the assumption that the optical depth is small compared to the

thermal boundary layer dimension, and that the depth of the domain is effectively infinite.

A main result for both surface boundary conditions is that the numerical analysis compares favorably with the linear thermal profile theoretical approximation for both the mid- and long-wave regimes. This more extensive analysis provides additional evidence that the previous theoretical model, approach, and attendant assumptions are reasonable and that Equation (8) provides insight to key parameters that control the signal strength.

However, it is important to note that the surface boundary condition and structure of the underlying thermal stratification may interact to control the signal strength. For a constant surface temperature state, representative signal strength varied as much as 200% for the mid-wave band and 250% for the long-wave region. We speculate that the source of the increase in signal strength may be traced directly to the structure of the thermal layer and its overlap with the optical depths for each waveband.

REFERENCES

- Atmane, M. A., Asher, W. E., and Jessup, A. T. (2004). On the use of the active infrared technique to infer heat and gas transfer velocities at the air-water free surface. *J. Geophys. Res.* 109:C08S14. doi: 10.1029/2003JC001805
- Chandrasekhar, S. (1960). *Radiative Transfer*. New York, NY: Dover Publications.
- Csanady, G.T. (2001). *Air-Sea Interaction: Laws and Mechanisms*. New York, NY: Cambridge University Press.
- Downing, H. D., and Williams, D. (1975). Optical constants of water in the infrared. *J. Geophys. Res.* 80, 1656–1661. doi: 10.1029/JC080i012p01656
- Fairall, C. W., Bradley, E. F., Rogers, D. P., Edson, J. B., and Young, G. S. (1996). Bulkparameterization of air-sea fluxes for tropical ocean-global atmosphere coupled-ocean-atmosphere response experiment. *J. Geophys. Res.* 101, 3747–3764. doi: 10.1029/95JC03205
- Fredriksson, S. T., Arneborg, L., Nilsson, H., and Handler, R. A. (2016b). Surface shear stress dependence of gas transfer velocity parameterizations using DNS. *J. Geophys. Res.* 121, 7369–7389. doi: 10.1002/2016JC011852
- Fredriksson, S. T., Arneborg, L., Nilsson, H., Zhang, Q., and Handler, R. A. (2016a). An evaluation of gas transfer velocity parameterizations during natural convection using DNS. *J. Geophys. Res.* 121, 1400–1423. doi: 10.1002/2015JC011112
- Garbe, C. S., Schimpf, U., and Jahne, B. (2004). A surface renewal model to analyze infrared image sequences of the ocean surface for the study of air-sea heat and gas exchange. *J. Geophys. Res.* 109:01802. doi: 10.1029/2003JC001802
- Gautschi, W. (1961). Recursive computation of the repeated integrals of the error function. *Mathemat. Comput.* 15, 227–232. doi: 10.2307/2002897
- Handler, R.A., and Judd, K.P. (2018). Analysis of infrared radiation at an air-water interface. *Front. Mech. Eng.* 4:5. doi: 10.3389/fmech.2018.00005
- Handler, R. A., Saylor, J. R., Leighton, R. I., and Rovelstad, A. L. (1999). Transport of a passive scalar at a shear-free boundary in fully developed turbulent open channel flow. *Phys. Fluids* 11, 2607–2625. doi: 10.1063/1.870123
- Handler, R. A., and Smith, G. B. (2011). Statistics of the temperature and its derivatives at the surface of a wind-driven air-water interface. *J. Geophys. Res. Oceans* 116:C6. doi: 10.1029/2010JC006496
- Handler, R. A., Smith, G. B., and Leighton, R. I. (2001). The thermal structure of an air-water interface at low wind speeds. *Tellus A.* 53, 233–244. doi: 10.3402/tellusa.v53i2.12187
- Handler, R. A., and Zhang, Q. (2013). Direct numerical simulations of a sheared interface at low wind speeds with applications to infrared remote sensing. *IEEE J. Select. Top. Appl. Earth Observ. Remote Sens.* 6, 1086–1091. doi: 10.1109/JSTARS.2013.2241736
- Herlina, H., and Wissink, J. G. (2014). Direct numerical simulation of turbulent scalar transport across a flat surface. *J. Fluid Mech.* 744, 217–249. doi: 10.1017/jfm.2014.68
- Jahne, B., Libner, P., Fischer, R., Billen, T., and Plate, E. J. (1989). Investigating the transfer processes across the free aqueous boundary layer by the controlled flux method. *Tellus* 41B, 177–195. doi: 10.3402/tellusb.v41i2.15068
- Jahne, B., Munnich, K. O., Bosinger, A. D., Huber, W., and Libner, P. (1987). On the parameters influencing air-water gas exchange. *J. Geophys. Res.* 92, 1937–1949. doi: 10.1029/JC092iC02p01937
- Katsaros, K. B., Liu, W. T., Businger, J. A., and Tillman, J. E. (1977). Heat transport and thermal structure in the interfacial boundary layer measured in an open tank of water in turbulent free convection. *J. Fluid Mech.* 83, 311–335. doi: 10.1017/S0022112077001219
- Kays, W. M., and Crawford, M. E. (1993). *Convective Heat and Mass Transfer*. New York, NY: McGraw-Hill.
- Leighton, R. I., Smith, G. B., and Handler, R. A. (2003). Direct numerical simulations of free convection beneath an air-water interface at low Rayleigh numbers. *Phys. Fluids* 15, 3181–3193. doi: 10.1063/1.1606679
- Liu, W. T., and Businger, J. A. (1975). Temperature profile in the molecular sublayer near the interface of a fluid in turbulent motion. *Geophys. Res. Lett.* 2:403. doi: 10.1029/GL002i009p00403
- McAlister, E. D., and McLeish, W. (1970). A Radiometric System for Airborne Measurement of the Total Heat Flow from the Sea. *Appl. Optics* 9, 2697–2705. doi: 10.1364/AO.9.002697
- McAlister, E. D., McLeish, W., and Corduan, E. A. (1971). Airborne measurements of the total heat flux from the sea during bomex. *J. Geophys. Res.* 76, 4172–4180. doi: 10.1029/JC076i018p04172
- McKeown, W., Bretherton, F., Huang, H. L., Smith, W. L., and Revercomb, H. L. (1995). Sounding the skin of water: sensing air/water interface temperature gradients with interferometry. *J. Atmos. Oceanic Technol.* 12, 1313–1327. doi: 10.1175/1520-0426(1995)012<1313:STSOWS>2.0.CO;2
- McKeown, W., and Leighton, R. (1999). Mapping heat flux. *J. Atmos. Ocean Tech.* 16, 80–91. doi: 10.1175/1520-0426(1999)016<0080:MHF>2.0.CO;2
- Nagaosa, R., and Handler, R. A. (2003). Statistical analysis of coherent vortices near a free surface in a fully developed turbulence. *Phys. Fluids* 15, 375–394. doi: 10.1063/1.1533071
- Nagaosa, R., and Handler, R. A. (2012). Characteristic time scales for predicting the scalar flux at a free surface in turbulent open-channel flows. *AICHE J.* 58, 3867–3877. doi: 10.1002/aic.13773

AUTHOR CONTRIBUTIONS

All authors listed have made a substantial, direct and intellectual contribution to the work, and approved it for publication.

- Smith, G. B., Volino, R. J., Handler, R. A., and Leighton, R. I. (2001). The thermal signature of a vortex pair impacting a free surface. *J. Fluid Mech.* 444, 49–78. doi: 10.1017/S0022112001005304
- Wanninkhof, R. (1992). Relationship between wind speed and gas exchange over the ocean. *J. Geophys. Res.* 97, 7373–7382. doi: 10.1029/92JC00188
- Wanninkhof, R. (2014). Relationship between wind speed and gas exchange over the ocean revisited. *Limnol. Ocean. Methods* 12, 351–362. doi: 10.4319/lom.2014.12.351
- Zel'dovich, Y. B., and Raizer, Y. P. (1966). *Physics of Shock Waves and High-Temperature Hydrodynamic Phenomena*. New York, NY: Academic Press.

Conflict of Interest Statement: The authors declare that the research was conducted in the absence of any commercial or financial relationships that could be construed as a potential conflict of interest.

Copyright © 2019 Judd and Handler. This is an open-access article distributed under the terms of the Creative Commons Attribution License (CC BY). The use, distribution or reproduction in other forums is permitted, provided the original author(s) and the copyright owner(s) are credited and that the original publication in this journal is cited, in accordance with accepted academic practice. No use, distribution or reproduction is permitted which does not comply with these terms.

APPENDIX

Here the symbol i used in Equations (9c) and (10d) and the expression for repeated integrals of the complementary error function (erfc) used to generate the powers of the integral operator are defined. The operator is defined as (Gautschi, 1961):

$$i = \int_x^\infty$$

where repeated applications to the complementary error function takes the form

$$i^n \text{erfc}(x) = \int_x^\infty i^{n-1} \text{erfc}(t) dt, \quad n = 0, 1, 2, \dots,$$

with $i^{-1} \text{erfc}(x) = \frac{2}{\sqrt{\pi}} e^{-x^2}$.

The general recurrence formula is

$$2ni^n \text{erfc}(x) = i^{n-2} \text{erfc}(x) - 2xi^{n-1} \text{erfc}(x), \quad (n = 1, 2, 3, \dots).$$